Shape Determination During Needle Insertion With Curvature Measurements

Jin Seob Kim, Jiangzhen Guo, Maria Chatrasingh, Sungmin Kim, and Iulian Iordachita, *Senior Member, IEEE*

Abstract— The determination of a flexible needle shape during the insertion is an important issue in minimally invasive surgery techniques. This is especially critical when considering conventional surgery procedures where a surgeon usually determines how to proceed needle insertion further based on the current needle trajectory inserted into tissue during biopsy and removal of malignant tissues in the body. In this paper, we propose a new method to determine the shape of a needle that is being inserted, together with the curvature measurement data obtained by fiber Bragg gratings (FBG) sensors inside the needle. This approach can be particularly advantageous to the situations where visual guidance (such as by ultrasound probes) is not easily applicable. The description of a needle shape is based on the elastic rod theory and Lie-group-theoretic approach. We also present the comparison between two different calibration methods, which have an impact on the quality of the results of the proposed method. In order to verify the proposed method, needle trajectories by the model are compared with experimental data obtained by image analysis, which in turn emphasizes the capability of the proposed method.

I. INTRODUCTION

Needle insertion is a widely-used technique in many medical areas such as injection, biopsy, and malignant tissue removal. From mid 2000, robotic technologies using a flexible needle have been developed [1]–[9]. Due to its flexibility, flexible needle steering is ideal for minimally invasive surgery in that it can minimize tissue damage during the insertion. On the other hand, flexible needle steering requires sophisticated techniques to accurately control and plan the needle trajectory, which in turn necessitates a good model for the needle steering. A pioneering work on the modeling includes kinematic modeling and planning of a flexible needle based on the assumption that the needle trajectory mimics motions of a unicycle and a bicycle [5], [6].

The determination of a flexible needle shape during the insertion is an important issue in minimally invasive surgery techniques. This is especially critical when considering that, in typical surgery procedures, a surgeon usually determines how to proceed needle insertion based on the current needle trajectory to achieve the goal such as biopsy and removal of malignant tissues in the body. In order to achieve a better

J. S. Kim and I. Iordachita are with the Department of Mechanical Engineering, Johns Hopkins University, Baltimore, MD 21218, USA {jkim115,iordachita}@jhu.edu

J. Guo and M. Chatrasingh are with the Laboratory for Computational Sensing and Robotics (LCSR), Johns Hopkin University, Baltimore, MD 21218, USA {jzguo,mchatra2}@jhu.edu

S. Kim is with the Department of Computer Science, Johns Hopkin University, Baltimore, MD 21218, USA sungminkim@jhu.edu (currently with Korea Institute of Machinery and Materials, Daegu, South Korea)

needle steering planning, numerous measurement techniques have been implemented such as ultrasound guidance [9], MRI-guidance [10], and FBG sensors [10]–[14]. Among them, we are particularly interested in FBG-sensor guidance because of its real-time sensing capacity, biocompatibility, and high accuracy. An FBG sensor consists of an optic fiber strain gauge which can detect wavelength shift due to mechanical deformation, hence can provide curvature data of a needle and a continuum robot. Owing to the advantages, FBG sensors have been widely used in medical applications [15]–[17]. Furthermore, FBG technology is particularly advantageous to the situations where visual guidance is not easily applicable.

In this paper, we propose a new method for determining the shape of a flexible needle with an asymmetric bevel tip which is inserted in tissue, in combination with measured curvature data by the FBG sensors. The proposed method includes a new model that is based on the general elastic rod theory and Lie-group-theoretic approach. One advantage of the model is that it enables to compute out-of-plane deformation and torsional deformation, which are small yet possible even during needle insertion without rotation. This will be greatly beneficial when it comes to needle insertion with complex shapes. Furthermore, this new model will be applicable to extremely flexible continuum robots such as catheters. As well as the model, the quality of FBG sensor data (i.e., effect of calibration methods) is also important. To that end, we consider two different calibration methods: by using beam theory [10] and by using grooves with constant curvatures (such as in [13]). Then we compare the results to investigate the effect of the calibration methods.

This paper is organized as follows. First, the model in the propose method is explained in Section II. In Section III we provide details on the calibration method and experiments on needle insertion, as well as image analysis. Then we present results on the needle shape determination with two different calibration methods in Section IV. Finally, we conclude in Section V.

II. THE METHOD

A. The Model

First, let us introduce notations and terminology. We treat a bevel-tipped flexible needle as an inextensible elastic rod of which the arclength is denoted as $s \in [0, L]$ where L is the length of the inserted needle. We attach a reference frame at each point along the needle (see Fig. 1). This reference frame is expressed with an element of $SE(3)$ (rigid body motions in 3D space): $g(s) = (R(s), \mathbf{r}(s)) \in SE(3)$ where
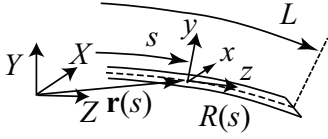
Fig. 1. Schematics the needle used in the model. The local reference frames attached the body point of the needle are shown.

$R(s) \in SO(3)$ (i.e. rotations in 3D space) and $\mathbf{r}(s) \in \mathbb{R}^3$. In particular, let us denote the tangent (insertion) direction of the needle coincident with the local z-axis of the reference frame attached to the points along the needle. Here we use Lie group theoretic approach [18], [19]. Let

$$\boldsymbol{\omega} = \begin{pmatrix} \omega_1 \\ \omega_2 \\ \omega_3 \end{pmatrix} = \left(R^T \frac{\partial R}{\partial s} \right)^\vee, \tag{1}$$

denote the angular deformation vector of a needle viewed from the reference frame attached to the point on the needle. We use this body-fixed description hereafter. Here $\vee$ operation defines a 3D vector associated with a 3×3 skew-symmetric matrix $R^T \frac{\partial R}{\partial s}$ [20], [21]. From our notations, ω_1 and ω_2 represent the curvature along the local x- and y-axes, whereas ω_3 denotes the torsion.

Now let us consider the insertion of a needle in more detail. As a needle is inserted, the needle deforms due to the force applied to the asymmetric bevel tip. Inside the tissue, the needle experiences forces from the ambient tissue such as distributed normal and shear forces along the needle. Such a variety of force effects on the needle have been considered in the modeling efforts [22], [23]. Furthermore, if we consider needle insertion as a quasi-static process which is suitable for our problem where we want to determine the shape of a needle that is inserted by L, then the distributed normal force along the needle can be considered the major component of the intrinsic deformation of the needle.

In an ideal needle insertion situation, the needle will deform according to the direction of the asymmetric bevel tip. Also the distributed normal forces along the needle will be exactly parallel to the local y-axis. Then the curvature direction along the needle should be the local x-axis in the current coordinate system (see Fig. 1). In other words, the needle will deform along this local direction only. This ideal deformation is effectively captured by introducing the intrinsic curvature, denoted as $\boldsymbol{\omega}_0 = [\kappa_0 \; 0 \; 0]^T$. Since $\boldsymbol{\omega}_0$ are due to distributed forces along the needle, κ_0 cannot be assumed constant in general. In order to explain the form of the intrinsic curvature, as an analogy, let us use classical beam theory. In the presence of uniformly distributed load q (see [24] for the justification of the uniform load for needle insertion), the moment is calculated as $M(x) = -\frac{1}{2}q(L - x)^2 = -\frac{1}{2}qL^2 \left(1 - \frac{x}{L}\right)^2$. Noting that $M(x) = EI\kappa_0$ where κ_0 denotes the curvature of the beam, this illustrates that the intrinsic curvature should be a function of arclength. Based on this analogy, we propose the intrinsic curvature

as a function of arclength in the following form

$$\kappa_0(s) = \kappa_c \left(1 - \frac{s}{L}\right)^2 \tag{2}$$

where $\kappa_c > 0$ is a parameter to be optimized. Note that, as can be inferred from the above consideration, κ_c is constant given L (i.e., κ_c can be a function of L; see Section IV for more discussion). In other words, in an ideal needle insertion situation, the deformation of the needle will be described by this intrinsic curvature. In the case of double-layered tissue with different material properties, by considering the same analogy from classical beam theory, we can use the following form of the intrinsic curvature

$$\kappa_0 = \begin{cases} \kappa_{c,1}\left(\frac{s^*-s}{L}\right)^2 + \kappa_{c,2}\left(1-\frac{s^*}{L}\right)\left(1+\frac{s^*}{L}-\frac{2s}{L}\right) & (0 \leq s \leq s^*) \\ \kappa_{c,2}\left(1-\frac{s}{L}\right)^2 & (s^* \leq s \leq L) \end{cases} \tag{3}$$

where $\kappa_{c,1}$ and $\kappa_{c,2}$ respectively denote the curvature parameters for each material. Here s^* denotes the arclength of the needle that corresponds to the width of the first layer, denoted as z^*. This s^* can be approximately determined as follows. First, compute the needle shape assuming one layer, i.e., only with $\kappa_{c,1}$. Then calculate z-coordinates and compare with z^* to select the corresponding arclength point which gives s^*.

Then this intrinsic curvature will serve as a reference that actual needle deformation should follow. Importantly, the intrinsic curvature is a coarse-grained representation of the environmental effects on the needle. Hence, our model is to minimize the following cost function

$$\mathcal{V} = \int_0^L \frac{1}{2} (\boldsymbol{\omega} - \boldsymbol{\omega}_0)^T B (\boldsymbol{\omega} - \boldsymbol{\omega}_0) \, ds \tag{4}$$

where $B \in \mathbb{R}^{3\times3}$ denotes the stiffness matrix as

$$B = \begin{pmatrix} EI & 0 & 0 \\ 0 & EI & 0 \\ 0 & 0 & GJ \end{pmatrix} \tag{5}$$

with EI and GJ being bending and torsional stiffness of a rod. Mathematically, we seek a curve $R(s) \in SO(3)$ that minimizes (4). Note that (4) is considered as elastic potential energy of a rod. This can be done by the variational calculus on Lie group which leads to the Euler-Poincaré equation as [18], [19]

$$B\frac{d}{ds}(\boldsymbol{\omega} - \boldsymbol{\omega}_0) + \boldsymbol{\omega} \times B(\boldsymbol{\omega} - \boldsymbol{\omega}_0) = \mathbf{0} \tag{6}$$

with the initial condition $\boldsymbol{\omega}_{\text{init}} = \boldsymbol{\omega}(0)$. This equation is to be solved together with

$$\frac{dR}{ds} = R\widehat{\boldsymbol{\omega}} \tag{7}$$

with the initial condition $R(0) = R_0$, where $\widehat{\boldsymbol{\omega}} \in so(3)$ (i.e., the set of 3×3 skew-symmetric matrices) denotes the 3×3 skew-symmetric matrix corresponding to vector $\boldsymbol{\omega}$. Then the position of the points along the needle is computed by

$$\mathbf{r}(s) = \int_0^s R(\sigma)\mathbf{e}_3 \, d\sigma \tag{8}$$

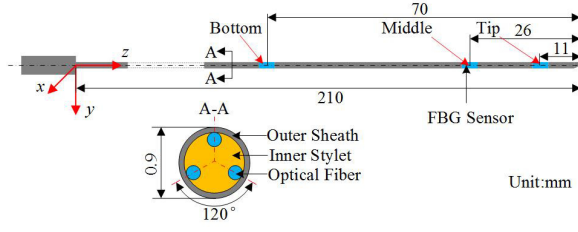due to the inextensibility condition of the needle.
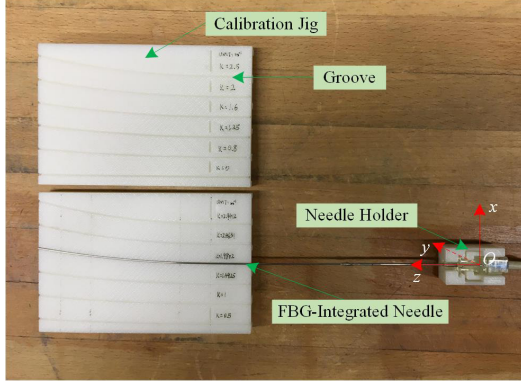
Fig. 2.   Design of a FBG-based sensorized needle

Fig. 3.   Experimental setup for the 'jig' calibration.

B. Optimization

The model is combined with the measurement data, denoted as a set of $\{\boldsymbol{\omega}_j^m\}$ ($j \in \mathbb{Z}$), from the FBG sensors. Mathematically, given a set of experimental data $\{\boldsymbol{\omega}_j^m\}$ ($j \in \mathbb{Z}$) from the FBG sensors, we minimize the following cost function

$$\mathcal{C}(\boldsymbol{\eta}) = \sum_{j=1}^{m} \left\{ \left(\omega_{j,1}^m - \omega_1(s_j) \right)^2 + \left(\omega_{j,2}^m - \omega_2(s_j) \right)^2 \right\} \quad (9)$$

to determine the needle shape. Here j denotes the measurement points on the needle. Note that the measured data only contain curvature values, not torsional deformation, which leads to (9).

In general, optimization of (9) requires the corresponding optimization variables as the initial values of $\boldsymbol{\omega}(s)$, denoted as $\boldsymbol{\omega}_{\text{init}}$ to solve (6), and κ_c. Hence the optimization variables are defined as $\boldsymbol{\eta} = [\boldsymbol{\omega}_{\text{init}}^T \ \kappa_c]^T$. Then we can utilize the optimization techniques to solve the minimization problem. In practice, we use "fmincon" in Matlab. This is especially true when we consider the needle insertion into a homogeneous tissue. However, in the case of multi-layered tissue, we can first perform the optimization on each homogeneous tissue to obtain the corresponding κ_c values, then finally we run the optimization only with $\boldsymbol{\omega}_{\text{init}}$ as the optimization variables.

III. EXPERIMENTS

A. Needle Calibration

A calibration was conducted to map the curvatures of the needle onto the wavelength shift of FBG sensors. Three FBG sensors are located inside the needle as shown in Fig. 2: 11, 26, and 70 mm away from the tip of the needle.

(a) Bottom, bent in yz-plane

(b) Bottom, bent in xz-plane

(c) Middle, bent in yz-plane

(d) Middle, bent in xz-plane

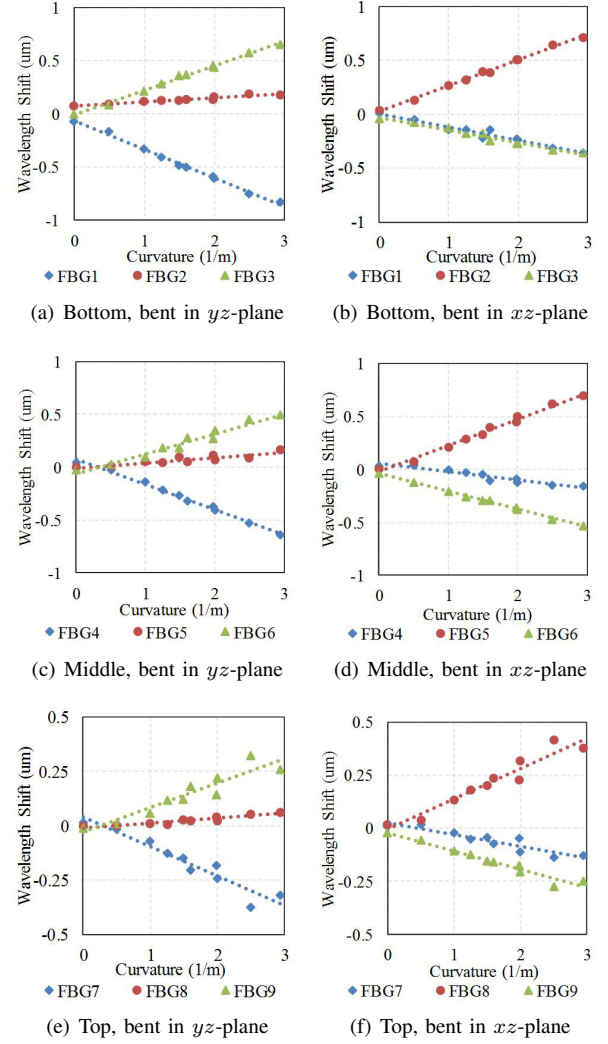(e) Top, bent in yz-plane

(f) Top, bent in xz-plane

Fig. 4.   Calibration results

These locations are determined according to the previous optimization study [10]. Fig. 3 presents the experimental setup for the calibration by using grooves. A reader can refer to [10] for the calibration by using beam theory. Two 3D-printed calibration jigs with 12 grooves of different curvatures that range between 0 and 2.9412 m^{-1} were designed. The curvature along each groove is constant. A needle holder was used to guarantee the same orientation of the needle when it was manually installed into different grooves. For monitoring the response of each FBG, we used an optical sensing interrogator, sm 130-170 from Micro Optics Inc. (Atlanta, GA), which provide a wavelength resolution of 1 pm.

During the calibration, the FBG-based sensorized needle was bent in two planes (yz- and xz-planes in Fig. 1) that are perpendicular with each other, and it was placed into each groove five times in each bending plane. The wavelength shift of each FBG sensor was read by the interrogator, recorded, and their mean values were calculated. The mean value then corresponds to the curvature of each groove. Fig. 4
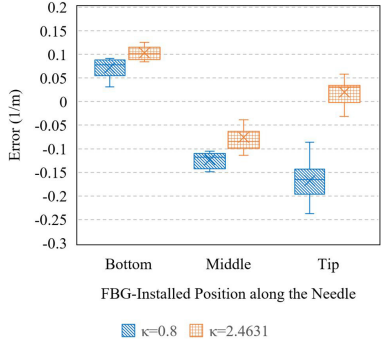
Fig. 5. Curvature validation errors

TABLE I

ERRORS OF CURVATURE VALIDATIONS

Position	Nominal Value [1/m]	Error [1/m]	
		mean	std
Bottom	0.8	0.0713	0.0208
Middle	0.8	-0.1235	0.0163
Tip	0.8	-0.1677	0.0433
Bottom	2.4631	0.1034	0.0143
Middle	2.4631	-0.0754	0.0389
Tip	2.4631	0.0198	0.0271

shows the FBG sensors' wavelength shift in three sections, at the bottom, middle, and tip of the needle, related to variable curvatures in two bending planes.

Fig. 4 indicates that the wavelength shift of each FBG sensor has an approximately linear relationship with its curvature. This relationship can be presented by the slope of the fitted lines as $\Delta\lambda_i = C_i[\kappa_{yz,i}, \kappa_{xz,i}]^T$. Here $\Delta\lambda_i$ is the wavelength shift vector at a position where three FBG sensors were installed, and $\kappa_{yz,i}$ and $\kappa_{xz,i}$ represent the curvatures in the yz- and the xz-plane (or along the x- and y axes) at the same position, respectively. C_i denotes the calibration matrix at each position. Since the FBG sensors were located in three positions of the needle, three calibration matrices from the bottom to the tip of the needle can be obtained as

$$C_1 = \begin{bmatrix} -0.2686 & 0.039 & 0.2295 \\ -0.1234 & 0.239 & -0.1156 \end{bmatrix}^T;$$

$$C_2 = \begin{bmatrix} -0.24 & 0.0498 & 0.1901 \\ -0.0779 & 0.2478 & -0.1699 \end{bmatrix}^T;$$

$$C_3 = \begin{bmatrix} -0.1355 & 0.0227 & 0.1128 \\ -0.0559 & 0.143 & -0.0871 \end{bmatrix}^T.$$

Using the pseudo-inverse of calibration matrices, the curvatures can be derived by the wavelength shifts of the FBG sensors. Bending the needle in yz-plane by two grooves with given curvatures of 0.8 m^{-1} and 2.4631 m^{-1} were conducted to validate the calibration. The bending procedure was repeated 10 times for each groove. The curvatures were first calculated based on the calibration matrices, and compared with actual values to obtain the errors, as presented in Table I and Fig. 5.
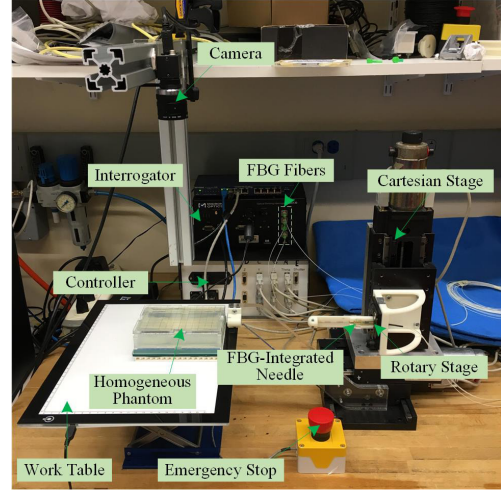

Fig. 6. Experimental setup for needle insertion.

The maximum magnitude of error averages and standard deviations are 0.1677 m^{-1} and 0.0433 m^{-1}, respectively, where the needle tip was bended in the groove with a curvature of 0.8 m^{-1}. These results illustrate that the curvatures along the needle can be generated by the calibration matrices and wavelength shifts of the FBG sensors.

B. Needle Insertion

To verify the shape determination of the needle during insertions, we established an experimental platform (Fig. 6). An isotropic phantom made of plastic (Super soft plastic from M-F Manufacturing Company, TX, US) was used to simulate soft tissue. Also an isotropic phantom made of Regular plastic 4:1 Hardener (same company) was used for hard tissue. An optical interrogator (sm 130-700 from Micron Optics Inc., Atlanta, GA) was used to collect the FBG-sensors' wavelength shifts. A manual rotary stage was used to carry the FBG-integrated needle, and installed on a three-degree-of-freedom Cartesian stage to adjust the initial position and to drive the needle into the phantom. An FL2-08S2C camera (Point Grey Research Inc., Richmond, BC, Canada) was fixed on the top of the phantom to capture images of the needle during insertions to provide ground truths. Ten needle insertions with a depth of 90 mm were conducted to validate the shape determination method.

C. Image Analysis of Needle Trajectories

The ground truth for the evaluation was defined by extracting needle trajectories from camera images. An FL2-08S2C camera (Point Grey Research Inc., Richmond, BC, Canada) was applied to capture the needle after inserting into phantom tissue. The dimension of each camera image is 1024×768 (pixels). To remove distortion in the camera images, Zhangs camera calibration method was applied to each captured image, which is implemented in the Camera Calibration Toolbox for Matlab distributed by Computational Vision lab at Caltech [25]. The coordinates on the image were generated with respect to the grid that was placed on the

TABLE II

κ_c (MEAN $\pm$ STANDARD DEVIATION)

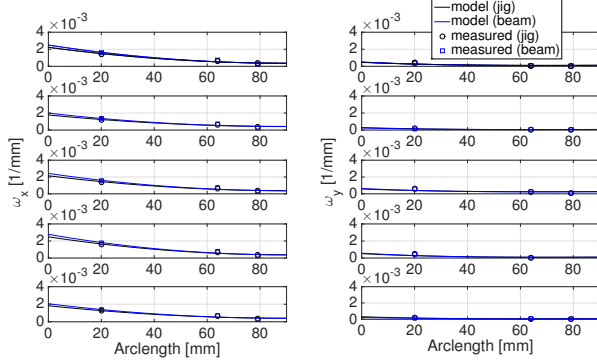| Calibration	soft phantom [1/mm]	hard phantom [1/mm]
jig	$0.0017 \pm 3.16 \times 10^{-4}$	$0.0027 \pm 4.00 \times 10^{-4}$
beam	$0.0020 \pm 3.40 \times 10^{-4}$	$0.0032 \pm 4.15 \times 10^{-4}$

Fig. 7. Plots of ω_x and ω_y selected from 10 trials of needle insertion into soft phantom tissue. Solid lines correspond to model results, whereas FBG sensor data are marked as circles and squares: black and blue respectively correspond to jig calibration method and calibration method based on the beam theory (color available online).

Fig. 8. An exaggerated figure explaining the initial rotation angle θ_0 due to the mis-alignment.

phantom before the needle insertion procedures where each 10 mm grid has 55 pixels. At first, needle was extracted using a threshold value (which is about 0.2 mm, i.e., error bound in the image process), and the center curve of the extracted region could be determined by using morphological skeleton operation. The curve was converted to the coordinates to match with the physical coordinates of the needle. Note that the needle shape measurements through camera imaging process are still prone to possible errors. For example, there might be errors from high refraction index of the phantom tissue, which will increase as the tissue becomes thicker. Hence further investigation on possible error sources might be necessary.

IV. RESULTS

First we performed needle insertion into a single layer of soft (Super soft plastic from M-F Manufacturing Company, TX, US) and hard (Regular plastic 4:1 Hardener, same company) phantom tissue. Length of an inserted needle segment for all experiments is 90 mm (i.e., $L = 90$ mm), as in Section III. As we specified, the optimization variables include κ_c and $\boldsymbol{\omega}_{\text{init}}$. We considered two different data sets by two calibration methods: jig calibration method (denoted as 'jig') and the calibration method based on the beam theory (denoted as 'beam') [10]. Table II shows the mean and the standard deviation of κ_c of soft and hard phantom tissue according to the 'jig' and 'beam' calibration methods.

Obtained curvature trajectories for soft phantom tissue are shown in Fig. 7. These figures show that the proposed method generates curvature trajectories that are in excellent agreements with the experimental data.
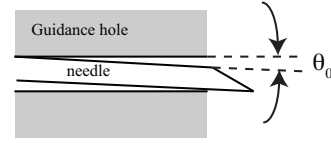
Then we moved on to the determination of needle shape. To that end, we included the effect of the so-called "initial rotation angle" (see Fig. 8). This phenomenon occurs due to the mis-alignment between needle shaft and the guidance hole, which can be caused either due to an asymmetric bevel tip, due to errors when inserting a needle, or both. This θ_0 impacts the initial rotation in the model: $R_0 = \text{Rot}_x(\theta_0)$ where Rot_x denotes the rotation about the x-axis. In the current model, we assume that this initial rotation angle θ_0 only occurs about the x-axis of the frame at the insertion point. In other words, the needle is inserted in a perfect manner such that the bevel tip surface does not rotate at the initial point. Also considering the fact that even though there is a mis-alignment, this initial angle should be very small (about 1~2°) because of the interaction between the needle (the diameter is 0.9 mm) and the guidance hole (the diameter is 1 mm and the length is about 6 mm). Apparently, θ_0 should vary in each trial. Hence, we performed the optimization on θ_0 based on the image data. Note that the purpose of the newly proposed method is to determine the shape of a needle mainly based on FBG curvature data, which currently renders it impossible to include this initial rotation angle as an optimization variable, which forms one of our future efforts.

Based on the aforementioned discussion, we performed the optimization given data sets. Fig. 9 shows five resulting needle trajectories selected from 10 trials with soft tissue together with the trajectories obtained by image analysis as explained in Section III-C for the verification of the proposed method. Also Table III presents the mean and standard deviation of errors. We consider two types: needle tip deflection and root-mean-square errors (RMSE) along the needle trajectories. Here RMSE is calculated as

$$\text{RMSE} = \sqrt{\frac{1}{M} \sum_{i=1}^{M} (y_i - y_i^{\text{m}})^2} \qquad (10)$$

where M denotes the number of points along the needle from image analysis. Here y_i and y_i^{m} denote y-coordinates obtained from the model and from the image data, respectively.

As shown in Fig. 9 and Table III, the model results are in excellent agreements with image data sets. In Table III, we show a quantitative comparison of model results between two calibration methods. Both calibration methods shows tip deflection error about 0.2 mm, which is the error bound of the image data. Regarding RMSE, both methods result in the order of 0.1 mm. For comparison, we applied the interpolation method based on the classical beam theory [10], which

TABLE III

ERROR STATISTICS (MEAN ± STANDARD DEVIATION) FOR SOFT
PHANTOM TISSUE

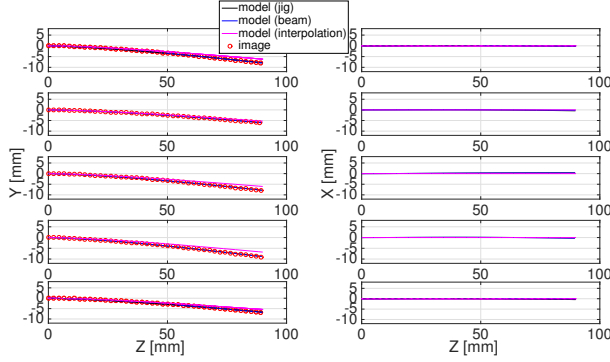|	Tip error [mm]	RMSE [mm]
model (jig)	0.1976 ± 0.1167	0.1439 ± 0.0329
model (beam)	0.1631 ± 0.0918	0.1138 ± 0.0255
interpolation	1.3693 ± 0.6457	0.6576 ± 0.3021

Fig. 9. Plots of needle shapes selected from 10 trials of needle insertion into soft phantom tissue. Black and blue solid lines correspond to model results based on FBG sensor data. Circles denote the position of the needle from the image analysis. In the left column, needle shapes in the yz plane are shown, In the right column, needle shapes in the xz plane are shown. For comparison, results from the interpolation method are shown.
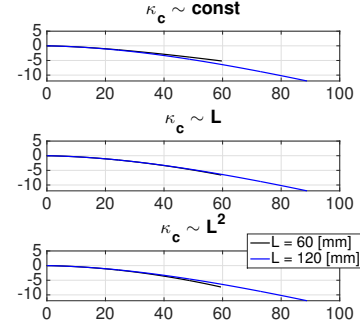

Fig. 10. The comparison of needle trajectories with different L values.
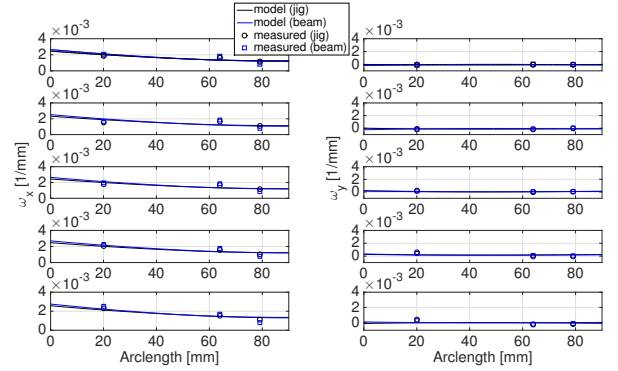

Fig. 11. Plots of ω_x and ω_y selected from 10 trials of needle insertion into double-layered phantom tissue (soft-hard). Solid lines correspond to model results, whereas FBG sensor data are marked as circles and squares: black and blue respectively correspond to jig calibration method and calibration method based on the beam theory (color available online).

clearly demonstrates that the proposed model improves the accuracy significantly. Results on hard phantom tissue draw the same conclusion. In total, the results emphasize that the proposed method can determine the needle shape more accurately. In addition, when we look at the right column in Fig. 9, which show the needle trajectories in xz plane, we can verify that the needle is indeed inserted in the yz plane (note that the interpolation method is not capable of predicting any out-of-plane (i.e, xz plane) deformation).

So far, we have considered needle insertion into a single homogeneous tissue. In order to verify our model further, we considered needle insertion into double-layered phantom tissue, where soft tissue (width $z^* = 45$ mm) is placed at the needle insertion point, and right next to it, hard phantom tissue is placed. $\kappa_{c,1}$ and $\kappa_{c,2}$ were chosen as the average values in Table II. Hence ω_{init} become the optimization variable in Section II-B. Also we performed the optimization on θ_0 as in the single-layered tissue cases.

We proposed the form of the intrinsic curvature as in (2) for single-layer needle insertion. In this form, κ_c is a constant given L. This is fine in the needle insertion into single-layered tissue ($L = 90$ mm). However, in the insertion of the needle into double-layered phantom tissue, lengths of the needle inserted into each layer will be different from 90 mm. Then we need to verify whether κ_c is constant over any L. This can be checked by noting the experimental results where needle trajectories are almost identical according to different insertion lengths of the needle into single-layered tissue. To that end, we tested three different scenarios: 1)

κ_c is constant over any L; 2) $\kappa_c \sim L$; 3) $\kappa_c \sim L^2$ (as in the beam theory analogy). Fig. 10 shows the model results of needle insertion into single layered tissue when $L = 60$ mm and $L = 120$ mm. The results clearly show that $\kappa_c \sim L$ should be the case in our model. Since κ_c's in Table II are obtained when $L = 90$ mm, $\kappa_{c,i}$ ($i = 1, 2$) in double-layered tissue, in (3), should be modified as $\kappa_{c,i} \to \kappa_{c,i}L_i/L$ where $L = 90$ mm, and L_i corresponds to needle insertion length of each layer.

Resulting curvature trajectories and needle shapes are shown in Fig. 11 and 12, respectively. Error statistics are shown in Table IV. Again, the proposed model shows excellent agreements with the measurements. This can also be confirmed in Table IV. One notable issue is out-of-plane deformation of the needle, as seen in the right column of

TABLE IV

ERROR STATISTICS (MEAN ± STANDARD DEVIATION) FOR
DOUBLE-LAYERED PHANTOM TISSUE

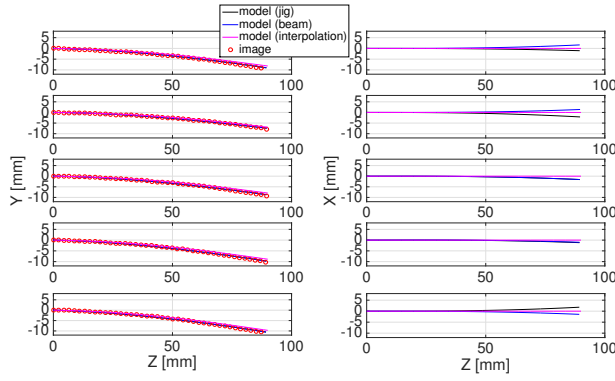|	Tip error [mm]	RMSE [mm]
model (jig)	0.4745 ± 0.1716	0.1969 ± 0.0311
model (beam)	0.4274 ± 0.1676	0.1806 ± 0.0297
interpolation	1.4970 ± 0.3013	0.6045 ± 0.1469

Fig. 12. Plots of needle shapes selected from 10 trials of needle insertion to double-layered phantom tissue (soft-hard). Black and blue solid lines correspond to model results based on FBG sensor data. Circles denote the position of the needle from the image analysis. In the left column, needle shapes in the yz plane are shown, In the right column, needle shapes in the xz plane are shown. For comparison, results from the interpolation method are shown.

TABLE V
θ_0 STATISTICS: MEAN (STANDARD DEVIATION)

	soft [°]	hard [°]	soft-hard [°]
jig	1.3423(0.3551)	1.7198(0.7107)	1.1870(0.5406)
beam	1.0594(0.3367)	1.2505(0.5783)	0.9594(0.5562)

Fig. 12. Since we lack 3D needle shape measurement, it is currently not available for us to compare the prediction with experimental data. This out-of-plane deformation is prominent in the second (hard) layer. One possible explanation on this is that even though we treat each layer as homogeneous material, in reality, there should be some degree of inhomogeneity. And the effect of material inhomogeneity on the needle shape will be more prominent as the material becomes stiffer. Although further investigation is required, the current results emphasize the potential of the proposed model on determining 3D needle trajectories.

From Table III and IV, one can see that the 'beam' calibration method exhibits a little better performance in terms of needle shape determination. However, when it comes to very flexible continuum robots and catheters, the 'jig' calibration method is expected to be more effective, considering that the 'beam' method has a difficulty when it comes to its application to extremely flexible rods.

Now let us investigate the statistics of θ_0, which is shown in Table V. One can see that the average values are small, as in our estimation based on the geometry of the needle guidance hole. In case of soft tissue, θ_0 is close to $1°$. In case of hard tissue, θ_0 becomes larger than the soft tissue case. This makes sense because the needle will tend to rotate more at the insertion point as tissue gets stiffer. The more interesting finding can be drawn from the comparison between the soft tissue and soft-hard tissue cases. Noting that both cases result in $\theta_0 \approx 1°$, this suggests that we can use θ_0 obtained from the tissue at needle insertion point no matter how many layers in the tissue. This gives us an

important clue on the further investigation on θ_0 for practical applications.

V. CONCLUSIONS

We presented a new method to determine the shape of a flexible bevel-tipped needle inserted in the tissue. In this method, we propose a new model based on the elastic rod theory and Lie-group-theoretic approach to describe the inserted needle. In the model, by introducing the intrinsic curvature which provides a reference needle deformation, we obtained the Euler-Poincaré equation. Then by combining with the FBG sensor data, the optimization was applied to determine the shape of the needle. Experiments were done on soft and hard single homogeneous phantom tissue and on double-layered phantom tissue (soft-hard). The results show that the proposed method could determine the needle shape accurately. This could also be verified by the comparison with the interpolation method. Another conclusion is that the 'beam' calibration performs better, albeit difference is negligible, in terms of the shape determination of a flexible needle. However we expect that the 'jig' calibration will be more useful when it comes to the application of the proposed method to much more flexible continuum robots such as catheters.

Apparently there are some limitations of the current work. First, we have considered simple needle insertion cases (i.e., C-shaped insertion). However, in reality, surgeons will need to halt the insertion, rotate and re-insert the needle into inhomogeneous tissue. Hence the application of the proposed method to more complex needle insertion cases (including rotations of the needle during the insertion and needle insertion into multi-layered materials) will be necessary. Second, currently planar needle trajectory measurements were considered. In order to truly appreciate the model capacity (i.e., capacity to predict out-of-plane needle deformation), we need 3D needle trajectory measurements (e.g., by using another camera or other image modalities such as ultrasound or X-ray imaging). All of these will be included in our future work, as well as further investigation on the initial angle and the path planning of a flexible needle. Finally, this method has a high potential to provide an effective and efficient approach to more general medical applications such as catheters for neurosurgery.

ACKNOWLEDGMENT

REFERENCES

[1] S. Okazawa, R. Ebrahimi, J. Chuang, S. E. Salcudean, and R. Rohling, "Hand-held steerable needle device," *IEEE/ASME Transactions on Mechatronics*, vol. 10, no. 3, pp. 285–296, 2005.
[2] S. P. Dimaio and S. E. Salcudean, "Needle steering and motion planning in soft tissues," *IEEE Transactions on Biomedical Engineering*, vol. 52, no. 6, pp. 965–974, 2005.

[3] J. A. Engh, G. Podna, S. Khoo, and C. Riviere, "Flexible needle steering system for percutaneous access to deep zones of the brain," in *Proceedings of IEEE Northeast Bioengineering Conference*, Easton, 2006, pp. 103–104.

[4] N. Abolhassani and R. V. Patel, "Deflection of a flexible needle during insertion into soft tissue," in *Proceedings of the International Conference on IEEE Engineering in Medicine and Biology*, New York, 2006, pp. 3858–3861.

[5] W. Park, J. S. Kim, Y. Zhou, N. J. Cowan, A. M. Okamura, and G. S. Chirikjian, "Diffusion-based motion planning for a nonholonomic flexible needle model," in *Proceedings of IEEE International Conference on Robotics and Automation*, 2005, pp. 4600–4605.

[6] R. J. Webster III, J. S. Kim, N. J. Cowan, G. S. Chirikjian, and A. M. Okamura, "Nonholonomic modeling of needle steering," *Int. J. of Robot. Res.*, vol. 25, no. 5–6, pp. 509–525, 2006.

[7] D. Glozman and M. Shoham, "Image-guided robotic flexible needle steering," *IEEE Transactions on Robotics*, vol. 23, no. 3, pp. 459–467, 2007.

[8] J. Rosen, B. Hannaford, and R. M. Satava, "Robotic needle steering: design, modeling, planning, and image guidance," *Surgical Robotics: Systems Applications and Visions*, no. August 2016, pp. 1–819, 2011.

[9] T. K. Adebar, A. E. Fletcher, and A. M. Okamura, "3D ultrasound-guided robotic needle steering in biological tissue," *IEEE Transactions on Biomedical Engineering*, vol. 61, no. 12, pp. 2899–2910, 2014.

[10] R. Seifabadi, E. E. Gomez, F. Aalamifar, G. Fichtinger, and I. Iordachita, "Real-time tracking of a bevel-tip needle with varying insertion depth: Toward teleoperated MRI-guided needle steering," *IEEE International Conference on Intelligent Robots and Systems*, pp. 469–476, 2013.

[11] R. J. Roesthuis, M. Kemp, J. J. van den Dobbelsteen, and S. Misra, "Three-dimensional needle shape reconstruction using an array of Fiber Bragg Grating sensors," *IEEE/ASME Transactions on Mechatronics*, vol. 19, no. 4, pp. 1115–1126, 2014.

[12] K. R. Henken, J. Dankelman, J. J. Van Den Dobbelsteen, L. K. Cheng, and M. S. Van Der Heiden, "Error analysis of FBG-based shape sensors for medical needle tracking," *IEEE/ASME Transactions on Mechatronics*, vol. 19, no. 5, pp. 1523–1531, 2014.

[13] S. C. Ryu and P. E. Dupont, "FBG-based shape sensing tubes for continuum robots," in *Proceedings of IEEE International Conference on Robotics and Automation (ICRA)*, Hong King, China, May 2014, pp. 3531–3537.

[14] R. Xu, A. Yurkewich, and R. V. Patel, "Curvature, torsion and force sensing in continuum robots using helically-wrapped FBG sensors," in *Proceedings of IEEE International Conference on Robotics and Automation (ICRA)*, Stockholm, Sweden, May 2016.

[15] L. Zhang, J. Qian, Y. Zhang, and L. Shen, "On SDM/WDM FBG sensor net for shape detection of endoscope," in *Proceedings of IEEE International Conference on Robotics and Automation*, vol. 4, 2005, pp. 1986–1991.

[16] I. Iordachita, Z. Sun, M. Balicki, J. Kang, S. Phee, J. Handa, P. Gelbach, and R. Taylor, "A sub-millimetric, 0.25 mm resolution fully integrated fiber-optic force-sensing tool for retinal microsurgery," *International Journal of Computer Assisted Radiology and Surgery*, vol. 4, no. 4, pp. 383–390, 2009.

[17] Y. Park, S. Elayaperumal, B. Daniel, S. C. S. C. Ryu., M. Shin, J. Savall, R. J. Black, B. Moslehi, and M. R. Cutkosky, "Real-time estimation of 3-D needle shape and deflection for mri-guided interventions," *IEEE/ASME Transactions on Mechatronics*, vol. 15, no. 6, pp. 906–915, 2010.

[18] D. D. Holm, J. E. Marsden, and T. S. Ratiu, "The Euler-Poincaré equations and semidirect products with applications to continuum theories," *Advances in Mathematics*, vol. 137, pp. 1–81, 1998.

[19] J. S. Kim and G. S. Chirikjian, "Conformational analysis of stiff chiral polymers with end-constraints," *Molecular Simulation*, vol. 32, pp. 1139 – 1154, 2006.

[20] G. S. Chirikjian and A. B. Kyatkin, *Engineering Applications of Noncommutative Harmonic Analysis*. CRC Press, 2001.

[21] G. Chirikjian and A. Kyatkin, *Harmonic Analysis for Engineers and Applied Scientists*. Dover, September 2015, (updated and expanded version of Engineering Applications of Noncommutative Harmonic Analysis, CRC Press, October 2000.).

[22] M. Abayazid, R. J. Roesthuis, R. Reilink, and S. Misra, "Integrating deflection models and image feedback for real-time flexible needle steering," *IEEE Transactions on Robotics*, vol. 29, no. 2, pp. 542–553, 2013.

[23] M. Khadem, C. Rossa, N. Usmani, R. S. Sloboda, and M. Tavakoli, "A two-body rigid/flexible model of needle steering dynamics in soft tissue," *IEEE/ASME Transactions on Mechatronics*, vol. 21, no. 5, pp. 2352–2364, 2016.

[24] M. Khadem, B. Fallahi, C. Rossa, R. S. Sloboda, N. Usmani, and M. Tavakoli, "A mechanics-based model for simulation and control of flexible needle insertion in soft tissue," in *Proceedings of IEEE International Conference on Robotics and Automation (ICRA)*, Seattle, Washington, May 26–30 2015, pp. 2264–2269.

[25] Z. Zhang, "A flexible new technique for camera calibration," *IEEE Transactions on Pattern Analysis and Machine Intelligence*, vol. 22, no. 11, pp. 1330–1334, 2000.